Chinese Journal of
POLYMER SCIENCE

RESEARCH ARTICLE

https://doi.org/10.1007/s10118-026-3801-8
Chinese J. Polym. Sci.

Transparent UV Cured Coatings Enabled by Biomass Phytic Acid with Enhanced Flame Retardancy and Low Temperature Toughness

Yu Yu[a,†], Sheng-Hua Yang[a,†], Hong-Yu Yuan[a], Feng Liu[a], Xia-Ming Feng[a,b*], Hong-Yu Yang[a,b*], and Chao-Jun Wan[a]

[a] *College of Materials Science and Engineering, Chongqing University, Chongqing 400044, China*
[b] *State Key Laboratory of Safety and Resilience of Civil Engineering in Mountain Area, Chongqing University, Chongqing 400044, China*

Electronic Supplementary Information

Abstract Ultraviolet (UV) curable transparent coatings are widely used in construction; however, achieving a balance between flame retardancy, transparency, and mechanical robustness, especially resistance to low-temperature brittleness, remains a challenge. Herein, we report a photocurable flame retardant coating system based on bis(methacryloyloxyethyl) phosphate (Bis-p) and bio-based phytic acid (PA). The coating preserved transparency (more than 85% visible-light transmittance) and a surface hardness (3H up to 10% PA), and maintained visible integrity in chemical immersion tests while improving mechanical performance. At −20 °C, the tensile strength and fracture toughness of PA5 were more than twice those of the control coating. It was found that sacrificial hydrogen bonds between the P—OH groups of PA and the Bis-p matrix contribute to reversible physical crosslinking. Under stress, hydrogen bonds break preferentially to dissipate energy, enhancing the toughness without compromising the integrity of the primary network. With increasing PA content, the limiting oxygen index increased from 29.5% to 34.5%. Samples with 10% and 15% PA achieved UL-94 V-0 rating. Cone calorimetry showed that, compared with PA0, PA15 reduced the peak heat release rate by 44.38%, smoke production rate by 48.37%, and CO production by 45.79%. An analytic hierarchy process (AHP) confirmed that PA15 reduced the overall fire risk. This study shows that introducing sacrificial hydrogen bonds through a bio-based additive offers a strategy for designing UV curable transparent coatings that overcome the trade-off between toughness and other essential properties.

Keywords Transparent coatings; Phytic acid; Flame retardancy; Mechanical properties; Hydrogen bonds

Citation: Yu, Y.; Yang, S. H.; Yuan, H. Y.; Liu, F.; Feng, X. M.; Yang, H. Y.; Wan, C. J. Transparent UV cured coatings enabled by biomass phytic acid with enhanced flame retardancy and low temperature toughness. *Chinese J. Polym. Sci*. https://doi.org/10.1007/s10118-026-3801-8

INTRODUCTION

UV-curable coatings are attractive for construction, automotive, and electronic applications because they cure rapidly, require low energy input, and can be formulated without solvents.[1,2] Transparent UV curable coatings are particularly useful for architectural applications because they protect wood, glass, and polycarbonate substrates while preserving their appearance.[3–5] However, most UV-curable resins are flammable, which limits their use in buildings with fire safety requirements.[6–9] Adding flame retardants is a common approach to improve fire resistance, but this often reduces the transparency and mechanical properties.[10–14] High loadings of conventional flame retardants can cause light scattering or phase separation, lowering the optical clarity.[15–19] In addition, highly crosslinked UV cured coatings tend to be brittle and crack easily, particularly at low temperatures, which restricts their outdoor use in cold climates.[20–22] The challenge is to improve both flame retardancy and toughness without losing transparency, hardness, or chemical resistance.[3,23,24]

Recent studies have attempted to combine optical transparency, flame retardancy, and mechanical robustness using different material designs. Ye *et al*. developed a thermally cured phosphorus/nitrogen-containing epoxy vitrimer with a transmittance of 85.9% at 700 nm, a toughness of 2.3 MJ/m^3, an LOI of 32.6%, and a UL-94 V-0 rating.[25] For UV-curable systems, Li *et al*. prepared cardanol-derived phosphorus-containing acrylate coatings that retained high transparency and achieved a tensile strength of 14.81 MPa, although low-temperature mechanical performance was not reported in that study.[24] Zhang *et al*. reported a biomimetic nanoporous fire-resistant coating with visible-light transparency above 97%, while Ma *et al*. obtained a transparent PLA/PHEMAP film with an LOI of 28% and a UL-94 V-0 rating at only 0.5 wt% PHEMAP.[26,27] These examples demonstrate several effective routes for balancing optical transparency and fire safety, including refractive-index matching, nanoporous structural design, and compatible phosphorus-containing networks.

* Corresponding authors, E-mail: fengxm@cqu.edu.cn (X.M.F.)
E-mail: yhongyu@cqu.edu.cn (H.Y.Y.)
† The authors contributed equally to this work.
Received May 18, 2026; Accepted July 3, 2026; Published online September 22, 2026

Nevertheless, mechanical reinforcement in transparent flame retardant systems is generally characterized at or near room temperature, and low-temperature toughness has rarely been reported. Dynamic hydrogen-bond networks have improved the tensile strength, self-healing capability, and fire safety of UV-curable polyurethane-urea acrylates and phytic-acid-containing thermoplastic polyurethane,[22,24,28] However these systems do not simultaneously address transparency, flame retardancy, and mechanical performance at sub ambient temperatures. Therefore, the behavior of transparent, highly crosslinked UV-curable flame-retardant coatings at −20 °C remains insufficiently understood.

In transparent UV-curable coatings, the rapid photopolymerization reaction creates highly crosslinked networks, that are inherently brittle.[29,30] As shown in this study, the unmodified Bis-p control (PA0) underwent brittle fracture at −20 °C and lost its mechanical integrity after UV aging. To address this, we used bio-based phytic acid (PA) to form a dynamically reversible sacrificial hydrogen-bond network with the Bis-p matrix. PA contains six phosphate groups (28 wt% P) and has been studied as a green flame retardant. The P—OH groups of PA can form hydrogen bonds with polar groups in the polymers. From a molecular perspective, the multiple P—OH groups of PA can act as hydrogen-bond donors, whereas the ester carbonyl and phosphoryl oxygen atoms in Bis-p can act as hydrogen-bond acceptors. Similar PA-mediated hydrogen-bonding interactions with carbonyl-containing polymer chains have been reported in PA-containing polyurethane and photopolymerized acrylic/acrylamide networks.[31] This offers a way to introduce reversible crosslinks that break under stress to dissipate energy and then re-form, enhancing the toughness without permanent damage to the network. A recent study by Huang *et al*. showed that PA can form a dynamic hydrogen bond network in thermoplastic polyurethane, improving both ductility and fire safety.[28] However, the incorporation of PA into highly crosslinked, phosphorus-rich UV curable systems, such as Bis-p has not been reported.

In this study, PA was incorporated into Bis-p UV-curable resin to construct a sacrificial hydrogen-bond network. This design was intended to enhance flame retardancy through the phosphate-rich structure of PA, preserve transparency through improved compatibility, suppress large-scale phase separation, and improve toughness at low temperatures through reversible energy-dissipating interactions while maintaining the hardness and chemical resistance required for coating applications. Coatings with different PA loadings were prepared and evaluated systematically. A multi-criteria analytic hierarchy process was further employed to assess overall fire safety.[32]

EXPERIMENTAL

Materials

Bis(2-(methacryloyloxy)ethyl) phosphate (Bis-p) was purchased from Bailingwei Technology Co., Ltd. (Beijing, China). A phytic acid solution (70 wt% in water) and 2-hydroxy-2-methylpropiophenone (purity ≥97%) were obtained from Shanghai Aladdin Biochemical Technology Co., Ltd. (Shanghai, China). A UV curing lamp (365 nm, 100 W) was supplied by the Zhongshan Tiandou Lighting Electrical Factory (Zhongshan, China). All chemicals were used as received, unless otherwise specified.

Preparation of Flame Retardant Coatings

Bis-p and phytic acid solutions were weighed according to the formulations listed in Table S1 (in the electronic supplementary information, ESI) and mixed in an aluminum foil cup. The mixture was degassed and dried in a vacuum oven at 50 °C for 1 h to remove the water and bubbles. After cooling to room temperature, 3 wt% of 2-hydroxy-2-methylpropiophenone was added, followed by thorough stirring and an additional 30 min degassing step. The mixture was poured into a 100 mm × 100 mm × 3 mm glass mold and cured under UV light for 60 s at room temperature. The samples are denoted as PA0, PA5, PA10, and PA15 according to the nominal PA content.

Characterization

Fourier transform infrared (FTIR) spectra were recorded on a Nicolet iS50 spectrometer using KBr pellets over the range of 4000–400 cm^{-1}. Variable-temperature FTIR was performed on a Shimadzu IR Tracer-100 instrument with a heating stage from 50 °C to 250 °C. Scanning electron microscopy (SEM) and energy-dispersive X-ray spectroscopy (EDS) images were obtained using a ZEISS Sigma 360 microscope. The samples were then sputter coated with gold. The limiting oxygen index (LOI) was measured on an HC-2 instrument according to ASTM D2863-97 using 100 mm × 6.5 mm × 3 mm specimens. UL-94 vertical burning tests (UL-94) were performed on a CZF-2 instrument following ASTM D3801 with a specimen size of 100 mm × 13 mm × 3 mm.

Thermogravimetric analysis (TGA) was carried out on a Mettler Toledo TGA2 under air or nitrogen at 30 mL/min from 25 °C to 800 °C at 10 °C/min. Cone calorimetry (CCT) was conducted according to ISO 5660 on a Suzhou Huichuan instrument at a heat flux of 35 kW/m^2 with a specimen size of 100 mm × 100 mm × 3 mm. TG-IR analysis was performed on a TGA Q5000 coupled with a Nicolet 6700 FTIR spectrometer under nitrogen at 20 mL/min from 25 °C to 800 °C at 20 °C/min. Raman spectra of the char residues were collected using a LabRAM HR Evolution microscope with a 532 nm laser. X-ray photoelectron spectroscopy (XPS) was performed using a Thermo Escalab 250 Xi instrument. Solid-state 31P CP/MAS NMR spectra were recorded to evaluate changes in the phosphorus chemical environment after curing. Atomic force microscopy (AFM) was used to examine the surface morphologies and phase structures of the cured coatings. Optical transmittance and haze spectra were measured to evaluate the transparency and light-scattering behavior.

Tensile tests were conducted on a CMT5105 universal tester at 2 mm/min according to GB/T 1447-2005 using dumbbell specimens, with each set of data representing the average of three replicates. The surface hardness was measured using pencil testers following GB/T 6739-2006 at (23±2) °C with 50 mm × 50 mm × 3 mm specimens. Transparency was evaluated using a Shimadzu UV-3600 spectrophotometer. Dynamic mechanical analyzer (DMA) testing: the storage modulus, loss modulus, and loss factor of the samples were measured using a DMA850 (TA Instruments, USA) instrument at a frequency of 1 Hz.

https://doi.org/10.1007/s10118-026-3801-8

RESULTS AND DISCUSSION

Characterization of Flame Retardant Coatings

Fig. 1(a) shows the preparation flowchart and schematic of the photocured microstructure, illustrating how PA forms hydrogen bonds with the Bis-p network. The FTIR spectra in Fig. 1(b) confirm the incorporation of PA. The C=O peak at approximately 1716 cm^{-1} from Bis-p remained unchanged, while the characteristic peaks of PA, including P=O at approximately 1155 cm^{-1} and P—O—C at approximately 973 cm^{-1} increased with increasing PA content. No additional covalent-bond-related peaks were observed, suggesting that PA interacted with the matrix primarily through hydrogen bonding rather than a chemical reaction.

Variable-temperature FTIR and two-dimensional (2D) correlation spectroscopy were used to probe the dynamics of the hydrogen bonds in PA10 as shown in Figs. 1(c) and 1(d).[33] At 25 °C, the synchronous spectrum exhibited a strong correlation between P=O vibrations in the range of 1150 –200 cm^{-1} and the C=O vibration region (1700–1750 cm^{-1}), indicating stable hydrogen bonding between the phosphate groups of PA and the carbonyl groups of Bis-p. As the temperature increased to 150 °C, the C=O bond shifted toward higher wavenumbers, which is consistent with the less hydrogen-bonded state. The P=O region also began to display free-state character, suggesting partial dissociation. The asynchronous spectrum at 150 °C displays cross-peaks between the phosphate and carbonyl regions.

According to Noda's rule for generalized two-dimensional correlation spectroscopy,[34] the signs of the synchronous and asynchronous cross-peaks at approximately 1155 and 1716 cm^{-1} suggest that the phosphate-associated band responds to heating before the carbonyl-associated band does. This sequential spectral response is consistent with the preferential perturbation and progressive weakening of PA-associated hydrogen-bonding interactions. When the DMA and tensile results are combined, these dynamic interactions may serve as sacrificial physical bonds that contribute to the energy dissi-

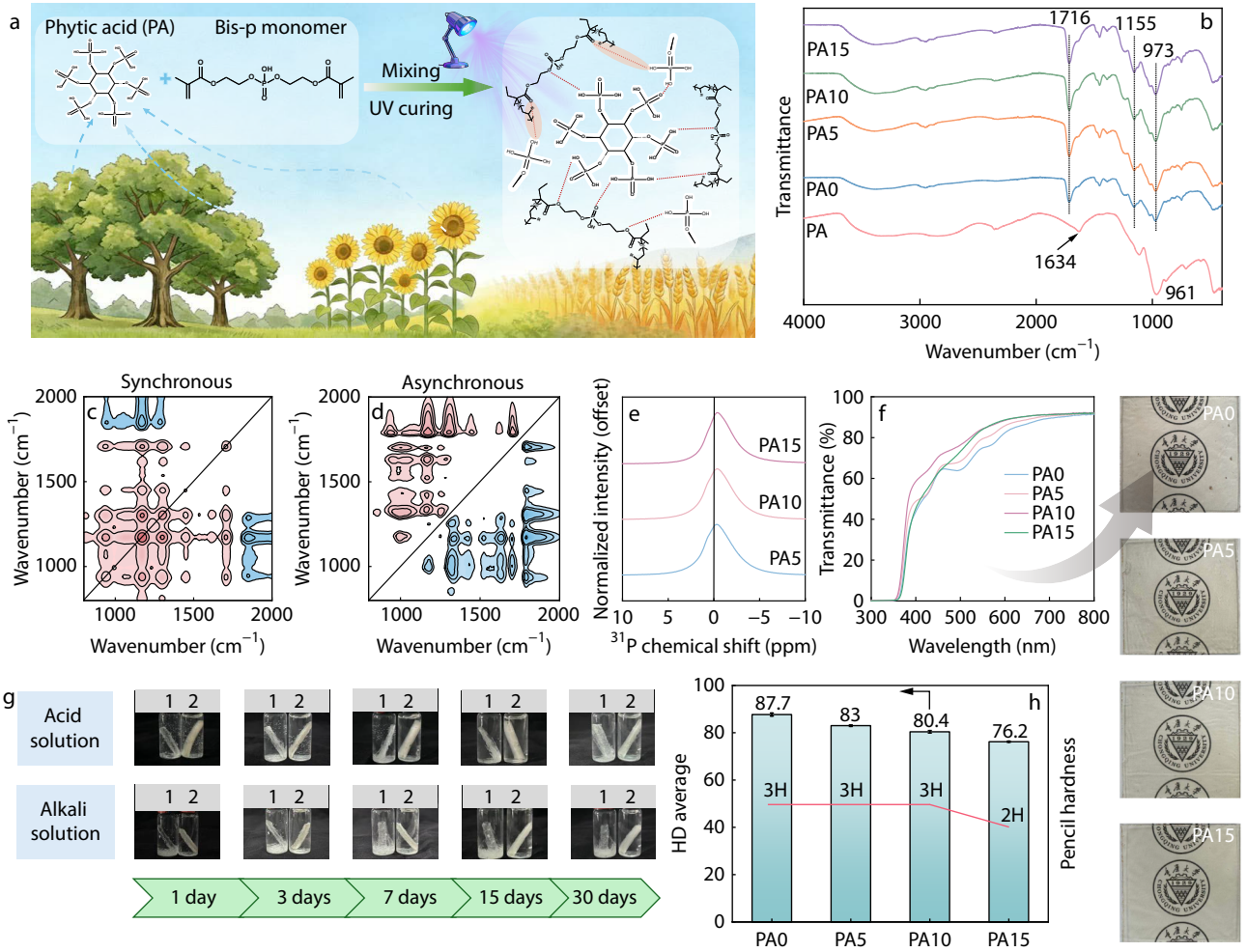

Fig. 1 (a) Schematic diagram of the synthesis mechanism, showing the formation of hydrogen bonds between PA and the Bis-p network; (b) FTIR spectra of PA additive, PA0, PA5, PA10, and PA15 samples; (c) Synchronous and (d) asynchronous 2D correlation FTIR spectra of PA10 sample during heating from 25 °C to 250 °C, revealing the sequential dissociation of hydrogen bonds; (e) Solid-state ^{31}P CP/MAS NMR spectra of PA5, PA10 and PA15; (f) UV-Vis spectra and photographs demonstrating the optical transparency of all samples; (g) Optical images of PA0 (label 1) and PA10 (label 2) after immersion in 1 mol/L HCl and 1 mol/L NaOH for 1, 3, 7, 15, and 30 days; (h) Pencil hardness and Shore hardness of PA0, PA5, PA10, and PA15 samples.

pation during deformation. It should be noted that variable-temperature FTIR analysis does not directly monitor the hydrogen bond dissociation during tensile deformation. Although PA0 also exhibited temperature-dependent cross-peaks (Fig. S1 in ESI), it lacked the PA-associated phosphate–carbonyl correlation observed in PA10, supporting the assignment of this additional dynamic interaction to the incorporation of PA.

Solid-state ^{31}P CP/MAS NMR was performed to examine whether PA generated a new phosphorus chemical environment after incorporation into the Bis-p network. As shown in Fig. 1(e), PA5, PA10, and PA15 exhibit similar ^{31}P resonances at approximately 0 ppm, and no additional phosphorus signal appears with increasing PA content. This result indicates that the phosphorus environment of PA was retained after its incorporation into the Bis-p network. To incorporate a functional modifier into a transparent coating, it is essential to determine whether the key properties of the base material are retained.

All the PA-containing coatings remained highly transparent, as shown in Fig. 1(f). The patterns on the back of the panels are clearly visible, indicating no marked increase in light scattering under the tested conditions. The UV-Vis spectra confirmed a high transmittance of more than 85% in the visible region. As shown in Fig. S2 (in ESI), the haze of all the coatings decreased with increasing wavelength, and PA15 exhibited the lowest haze across the visible region, indicating that the increased PA content did not induce severe light scattering and that good optical clarity was maintained. As shown in Fig. S3 (in ESI), this high transparency was maintained even after 60 h of UV-aging testing. The hydrogen-bonding interactions improved the compatibility between PA and the Bis-p matrix and suppressed continuous micron-scale phase separation under the tested conditions.

As shown by the AFM results in Fig. S4 (in ESI), PA5 possesses a relatively uniform surface with only a small number of isolated protrusions. In contrast, PA10 exhibits local protrusions and depressions with a distinct phase contrast, which reflects local surface inhomogeneity or mild aggregation of the material. PA15 features more severe surface undulation and higher roughness, yet no continuous micron-scale phase-separated domains are observed in its phase image. Even at 15 wt% PA loading, no continuous micron-scale separated domains were captured in the phase images, which explains why PA15 still maintained low haze and high transmittance without obvious light scattering.

The chemical tolerance was evaluated by immersing the samples in 1 mol/L HCl and 1 mol/L NaOH for up to 30 days, and images were recorded after 1, 3, 7, 15, and 30 days, as shown in Fig. 1(g). The PA0 coating exhibited visible degradation and discoloration, whereas PA10 retained its macroscopic appearance throughout the test. A similar visual retention was observed after exposure to the selected organic solvents, as shown in Fig. S5 (in ESI). This behavior is consistent with enhanced network integrity associated with hydrogen bonding and improved matrix compatibility. In Fig. 1(h), pencil hardness was 3H for PA0–PA10 and decreased to 2H for PA15. Shore hardn-ess decreased from 87.7 to 76.2 with increasing PA content, consistent with plasticization.

Mechanical Properties

DMA was used to evaluate the effect of PA on the viscoelastic behavior of the cured coatings. As shown in Fig. 2(a), the storage moduli of the samples decreased across the test temperature range as the PA content increased. At room temperature, the storage modulus of PA0 was 2121.0 MPa, whereas that of PA15 dropped to 721.9 MPa. This indicates that the small PA molecules disrupted the original crosslinked network, leading to a reduction in the dynamic stiffness of the coatings. The loss modulus curves in Fig. 2(b) reflect the evolution of the viscous response of the coating. As the PA content increased, the loss modulus exhibited an overall downward trend across the test temperature range, suggesting that the introduction of PA molecules reduced the internal frictional resistance between the polymer chains. This is consistent with the plasticizing effect of PA, whereby PA weakens the strong crosslinking within the polymer matrix, increases the free volume of the system, and promotes the relaxation movement of the polymer segments under heat.

The tanδ curves in Fig. 2(c) show that with the introduction of PA, the loss peak increased, while the glass transition temperature (T_g) shifted toward lower temperatures. This confirmed that the plasticizing effect of PA enhanced the mobility and viscoelastic response of the polymer chains. As shown in Fig. 2(d), as the PA content increases, the crosslinking density of the coatings decreases, while the molecular weight between the crosslinking points increases, providing structural evidence for the formation of a plasticized network.

As shown in Fig. 2(f) owing to plasticization of the network structure, the peak stress at room temperature decreased with increasing PA content. The fracture toughness values for the samples are as follows: PA0 at 1.05 MJ/m^3, PA5 at 1.12 MJ/m^3, PA10 at 0.95 MJ/m^3, and PA15 at 0.91 MJ/m^3. This indicates that the addition of PA did not significantly decrease fracture toughness. Meanwhile, the elongation at break gradually increased, exhibiting the characteristics of reduced strength and enhanced ductility. It is worth noting that at a low temperature of −20 °C, as shown in Figs. 2(e) and 2(g), all samples containing PA outperformed the control sample in terms of tensile strength and fracture toughness. Specifically, samples with the PA additive exhibited tensile strengths that were more than double that of the PA0 sample. The tensile strength and fracture toughness of PA5 were 2.24 and 2.16 times those of PA0, respectively. Demonstrating that PA effectively suppressed cold brittleness and improved low-temperature toughness. At −20 °C, segmental mobility in the highly crosslinked PA0 network was strongly restricted, leading to stress concentration and brittle fracture.

The incorporation of PA reduces the effective crosslink density and introduces reversible phosphate–carbonyl hydrogen bonds. Under load, these weaker physical interactions can dissociate before rupture of the covalent network, thereby dissipating energy and delaying crack propagation, whereas the permanent network preserves macroscopic integrity. The enhanced tensile strength and fracture toughness of PA5 and PA10 at −20 °C, together with the DMA and variable-temperature FTIR/2D-correlation results, are consistent with this sacrificial bond mechanism. Nevertheless, the FTIR experiment probes thermal perturbation rather than bond dissocia-

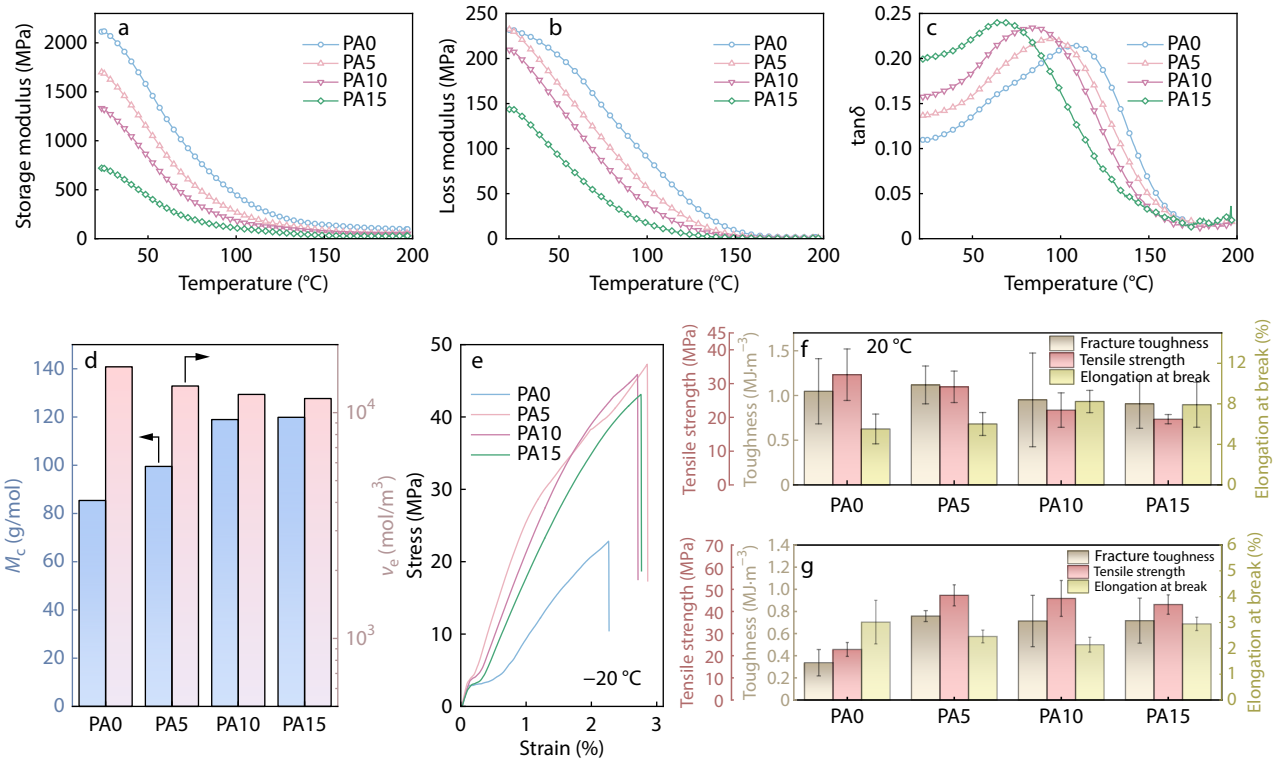

Fig. 2 (a) Storage modulus, (b) loss modulus, and (c) loss factor (tanδ) curves as a function of temperature for PA0, PA5, PA10, and PA15 samples; (d) Crosslink density (v_e) and molecular weight between crosslinks (M_c) for transparent coatings as functions of PA content; (e) Typical tensile stress-strain curves for all samples at −20 °C; (f) Room temperature tensile strength, fracture toughness, and elongation at break for all samples; (g) Tensile strength, fracture toughness, and elongation at break for all samples at −20 °C.

tion during tensile deformation; therefore, the mechanistic interpretation is presented as evidence-supported rather than direct *in situ* proof. After 24 h of UV aging, PA5 and PA10 retained tensile strengths close to or above their initial values, whereas PA15 showed a lower retention ratio (Fig. S6 in ESI), indicating that moderate PA loadings provided a more favorable balance between the initial strength and short-term aging resistance.

Flame Retardancy and Mechanism

TGA was used to compare the thermal-decomposition behavior of the coatings under air and nitrogen atmospheres (Fig. S7 in ESI).[35] The PA-containing samples began to decompose at slightly lower temperatures than PA0, while their peak mass-loss rates were reduced. Under nitrogen, the residual mass at 800 °C increases with increasing PA content. These results indicate that PA promotes earlier decomposition but favors char formation at elevated temperatures.

The UL-94 vertical burning test results, shown in Fig. 3(a), illustrate that the unmodified PA0 sample burned with dripping and received no rating. In contrast, the samples with 10% and 15% PA achieved a V-0 rating with immediate self-extinguishing and no dripping. As shown in Fig. 3(b), the LOI values progressively increased with increasing PA content, demonstrating the flame-retardant efficacy of PA. The LOI increased from 29.5% in the control sample to 34.5% with 15% PA loading. This 5.0-percentage-point increase placed PA15 in the self-extinguishing category. This indicates that a relatively modest PA loading of 10% was sufficient to impart the highest flame-retardant classification. The photographic sequences in Figs. S8 and S9 (in ESI) show that PA10 and PA15 self-extinguished after two flame applications after 24 h of UV aging, with no obvious flaming dripping visible in the recorded images.

Cone calorimetry provided quantitative insights into the combustion behavior under forced flame conditions, as shown in Figs. 3(c)–3(h). These results demonstrate that the flame-retardant action of PA is multifaceted. In general, a higher PA loading led to lower heat release and smoke production. Specifically, compared to the control PA0 sample, the 15% PA formulation reduced the peak heat release rate by 44.38%, smoke production rate by 48.37%, total smoke production by 34.27%, and CO production by 45.79%. These substantial reductions demonstrate that the sacrificial hydrogen bond network does not interfere with the char-forming process, which underpins flame retardancy and may even enhance it.

The char residues after cone calorimetry revealed a progressive change in the char morphology with increasing PA content. PA0 produced a fragmented and porous residue, whereas the PA15 char was smoother and more continuous (Fig. 4a and Fig. S11 in ESI). The intermediate samples showed the same trend: PA5 retained a more porous structure, whereas PA10 formed a denser and more continuous char layer (Fig. S11 in ESI). EDS mapping further showed that phosphorus was distributed throughout the PA-containing residues, which is consistent with the presence of phosphorus-contain-

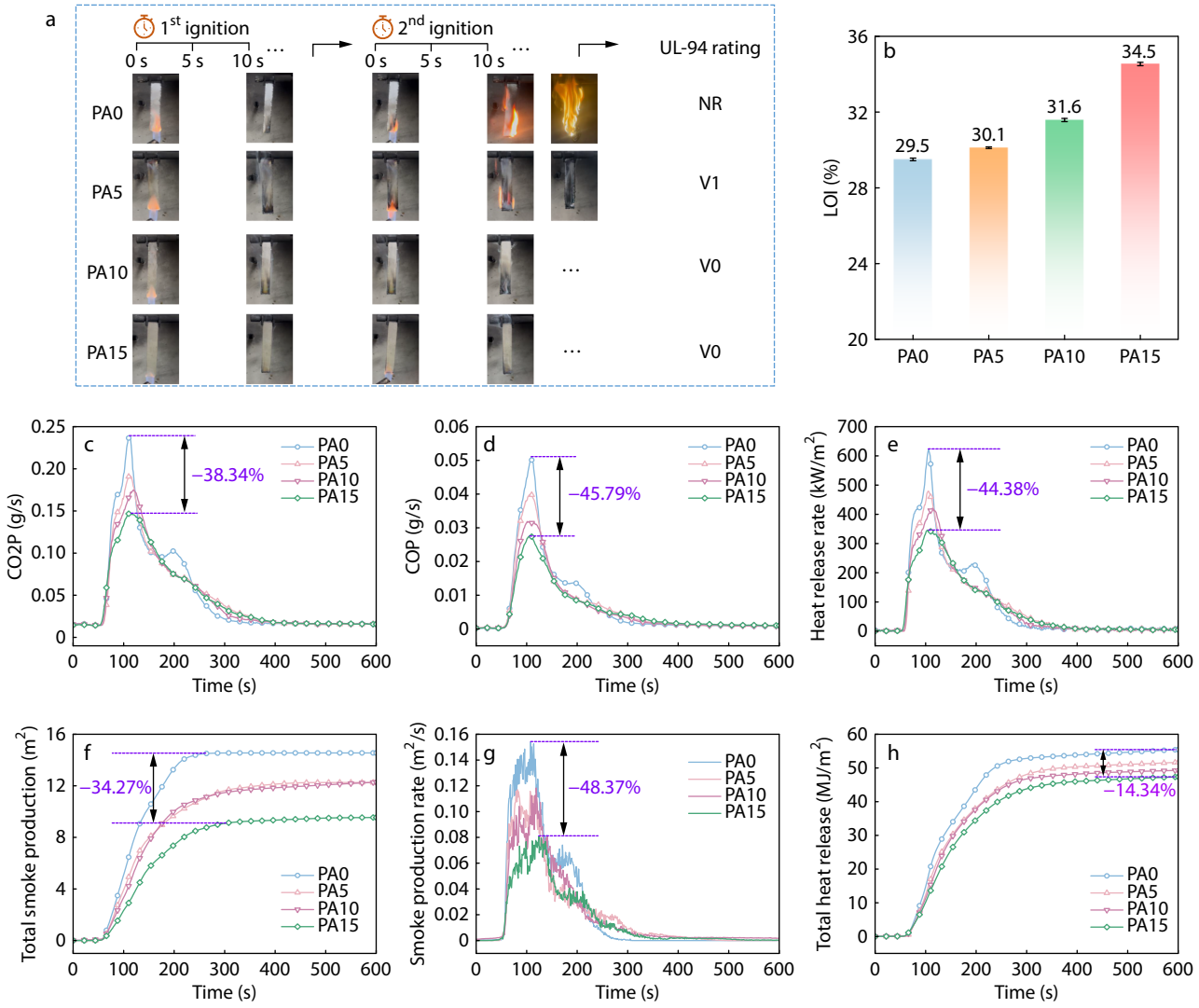

Fig. 3 (a) Snapshots from UL-94 vertical burning tests of PA0, PA5, PA10, and PA15; (b) LOI values for all samples; (c) CO_2 production rate (CO2P), (d) CO production rate (COP), (e) heat release rate, (f) total smoke production, (g) smoke production rate, and (h) total heat release from cone calorimetry for all samples.

ing species in the condensed-phase char.

XPS analysis provides more detail, as shown in Figs.4(b), 4(c) and Fig. S12 (in ESI). The PA15 char shows a stronger P 2p signal than PA0, again confirming phosphorus enrichment. The C 1s spectra show that both chars contain graphitic carbon, indicated by the peak at 284.8 eV, but the proportion is higher in PA15. This indicates better graphitization, which is consistent with the lower I_D/I_G ratio observed in Raman spectra, as shown in Figs. S10(i)–S10(l) (in ESI). More graphitic carbon means better thermal stability. The P 2p spectrum for PA15 shows peaks around 133.8 eV, which correspond to polyphosphates or phosphate esters, the kinds of compounds that form a glassy protective layer. The same hydrogen bonds identified above appear to play a role in char formation. When heated, these bonds break in a controlled way, allowing PA to redistribute and react with the decomposing Bis-p matrix. It explains why even 15% PA produces such a uniform char, as the hydrogen bonds keep PA well-dispersed until they are needed.

Thermogravimetry-infrared (TG-IR) spectroscopy was used to observe the volatiles released during decomposition. The 3D spectra in Figs. 4(d) and 4(e) show that PA15 releases much fewer total volatiles than PA0. The main products, including hydrocarbons, CO_2, carbonyls, and aromatics, were the same in both samples, as shown in Figs. 4(f) and 4(g). These results suggest that PA mainly reduces the evolution of combustible volatile products, rather than fundamentally changing the decomposition pathway. The absorbance profiles in Fig. 4(h) further demonstrate the suppressed evolution of total volatiles, CO, and hydrocarbons from PA15 compared with PA0, which is consistent with the 45.79% and 38.34% reductions in CO and CO_2 production, respectively, observed by cone calorimetry. Notably, this gas-phase suppression occurs in tandem with the condensed-phase mechanism. The formation of a dense char layer physically impedes the volatilization of combustible gases, thereby reducing the fuel supply to the flame. This demonstrates the synergistic flame-retardant effect originating from a single structural fea-

https://doi.org/10.1007/s10118-026-3801-8

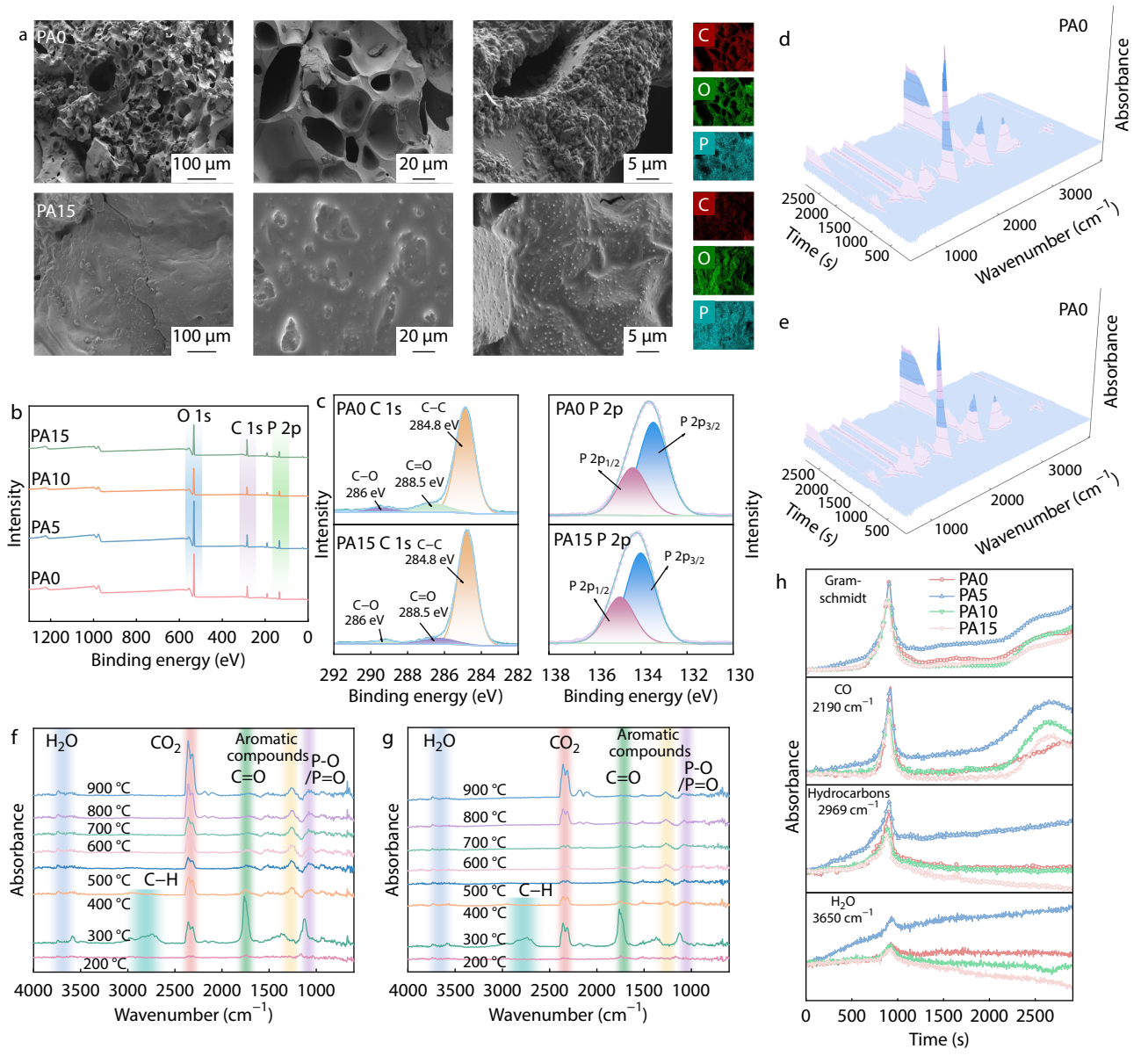

Fig. 4 (a) SEM images of char residues after cone calorimetry for PA0 and PA15, with corresponding EDS mapping results; (b) XPS survey and (c) high-resolution C 1s and P 2p XPS spectra of char residues for PA0 and PA15 samples; TG-IR 3D spectra of volatiles released during decomposition of (d) PA0 and (e) PA15 samples; FTIR spectra of volatiles at different pyrolysis temperatures for (f) PA0 and (g) PA15 samples; (h) Absorbance of total volatiles, CO, hydrocarbons, and H_2O as functions of time/temperature for all transparent coatings.

ture. The PA5 and PA10 spectra in Fig. S13 (in ESI) contain H_2O, CO_2, hydrocarbon, carbonyl, aromatic, and phosphorus-containing signals at the selected temperatures, indicating that the intermediate formulations produced the same major classes of volatile products.

To further assess the practical fire protection performance, two fire simulation tests were conducted. Wood panels coated with PA0 and PA15 at a thickness of 2 mm were exposed to a gas burner flame on the coated side, and the backside temperature was monitored, as shown in Figs. 5(a) and 5(b). After the same burning time, the backside of the PA15-coated panel was significantly cooler, indicating that the char layer acted as a thermal barrier. Small wooden houses, including one uncoated house, one coated with PA0, and one coated with PA15, had a flame applied to the same spot on each roof for 30 s and then removed, as shown in Figs. 5(c)–5(e). The uncoated house continued to burn until it was completely destroyed. Both coated houses self-extinguished within 5 s. However, it is clear that the roof of the house coated with the PA0 coating was burned through, forming an obvious hole. This indicates that the protective effect of the PA0 coating was limited. The PA15-coated house had a more intact char layer at the ignition site, which adhered to the wood and prevented reignition. These results verify the practical viability of the coating in realistic fire scenarios.

Multi-criteria Evaluation

No single fire-performance metric can comprehensively represent material fire safety. A material might have a high LOI but

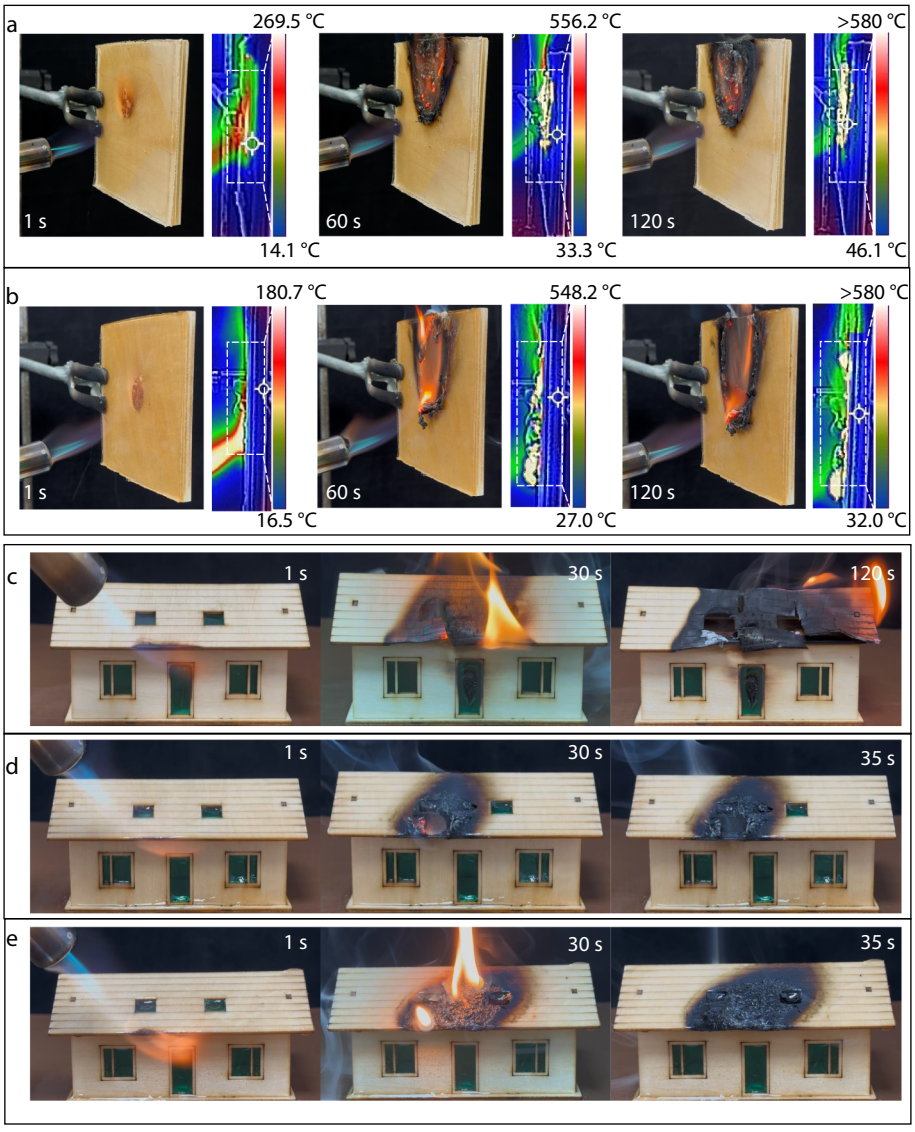

Fig. 5 Backside temperature measurement during direct flame test on wood panels coated with (a) PA0 and (b) PA15 coatings; (c) Uncoated wooden house after 30 s flame application, showing continued burning and destruction; (d) PA0-coated house after flame removal, self-extinguished with moderate char formation; (e) PA15-coated house after flame removal, showing intact char layer adhered to wood and superior protection.

produce large amounts of smoke, or it might self-extinguish in the UL-94 test but release toxic gases. To obtain a complete picture, we used the analytic hierarchy process (AHP) to combine 12 different measurements into one overall score, as shown in Fig. 6(a).[36] We assigned weights to each parameter based on what matters the most for safety. Toxic production received the highest first-level weight, followed by ignition and spreading, heat release, smoke production, and thermal stability. The weight assignments were checked for consistency, and all consistency ratios were below 0.1, as shown in Tables S2–S7 (in ESI). All the data were normalized to a scale of 0.1 to 1.0, so that different units could be compared.[37–39]

The AHP results are shown in Figs. 6(b)–6(e). Overall, fire safety increased with PA content, with PA15 scoring the highest. Looking at the individual components in Figs. 6(d) and 6(e), PA15 obtained near-perfect scores for the most important parameters, namely, peak CO production and peak heat release rate. This result suggests that the dense char barrier we identified was the main reason for improved safety. PA15 scored lower on thermal stability, for example, onset temperature, because PA catalyzed earlier degradation. This is a common trade-off in phosphorus flame retardants. However, because the thermal stability was weighted low at 6.4% in our model, it did not outweigh the gains in toxicity and heat release. The radar chart in Fig. 6(e) shows a shift from a spiky profile for PA0, which is good in some ways but bad in others, to a balanced profile for PA15, which is good across the board. Benchmarking against other flame-retardant systems, as shown in Fig. 6(f), indicates that PA10 compares well, with a high LOI, low peak heat release rate, excellent transparency, and the added benefits of solvent-free processing and rapid curing.[40–45] Thus, the AHP analysis quantitatively confirms

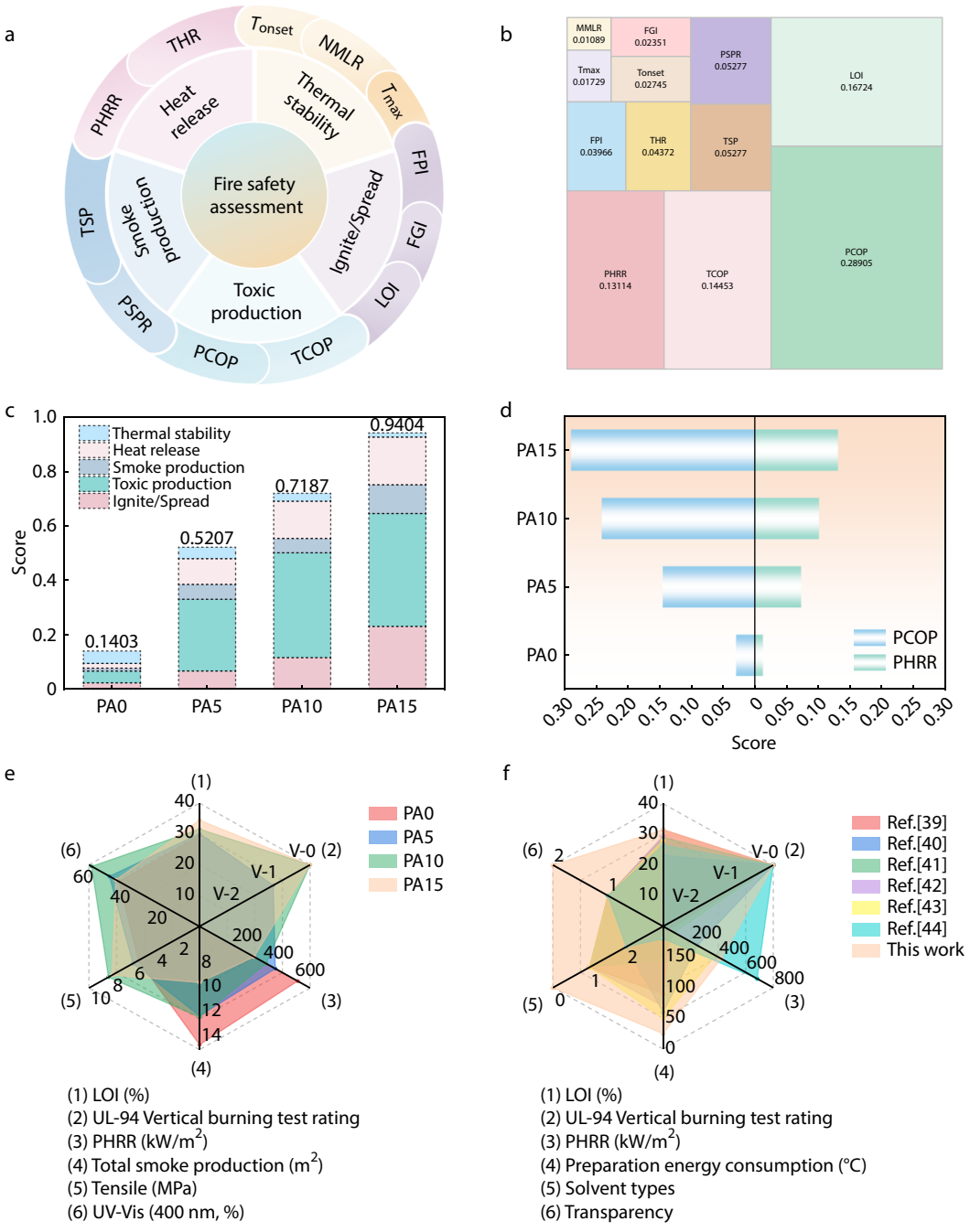

Fig. 6 (a) Twelve fire safety metrics used in the AHP model, covering ignition, heat release, smoke, toxicity, and thermal stability parameters; (b) Weight distribution of each metric based on life safety priorities; (c) Comprehensive fire safety scores of PA0, PA5, PA10, and PA15, showing progressive increase with PA content; (d) Normalized scores for the highest-weighted parameters, peak CO production (PCOP) and peak heat release rate (PHRR); (e) Radar chart comparing performance profiles of all samples; (f) Benchmarking of PA10 sample against other flame retardant systems from recent literatures, highlighting its high LOI, low PHRR, excellent transparency, and solvent-free rapid photocuring process.

that PA incorporation improves the fire-safety parameters most relevant to practical risk reduction. A one-at-a-time sensitivity analysis further showed that increasing or decreasing each first-level criterion weight by 20% did not change the AHP ranking, with PA15 remaining the top-ranked formulation in all scenarios (Table S12 in ESI), confirming that the fire-safety conclusion is robust within the tested weighting range.[46]

CONCLUSIONS

A transparent UV-curable flame-retardant coating was developed by incorporating bio-based PA into a Bis-p photocurable resin. The design exploits sacrificial hydrogen bonds between the P—OH groups of PA and the Bis-p matrix. These reversible physical crosslinks coexist with the permanent covalent networks. The variable-temperature FTIR, 2D-correlation, DMA, and tensile results support a sacrificial hydrogen-bond mechanism

that contributes to energy dissipation. Under low-temperature tensile loads, these dynamic hydrogen bonds preferentially dissociate to relieve concentrated stress and block crack extension, which distinguishes this mechanically activated bond cleavage from the thermally induced dissociation captured by FTIR and fully rationalizes the doubled tensile strength and fracture toughness of PA-modified coatings at −20 °C. AFM and optical analyses indicated that PA incorporation did not produce continuous micron-scale phase-separated domains, allowing the coatings to maintain a visible-light transmittance above 85%. The pencil hardness remained at 3H up to a PA loading of 10%. PA can promote the formation of dense, phosphorus-rich, graphitized char during combustion, which serves as a physical barrier. The LOI increases from 29.5% for PA0 to 34.5% for PA15. PA10 and PA15 attained UL-94 V-0 ratings. Compared to PA0, PA15 significantly reduced the heat release and smoke production. A multi-criteria evaluation based on AHP confirms that PA15 enhances overall fire safety, achieving near-perfect scores for the highest-weighted parameters of peak CO and peak heat release rate. This research demonstrates that introducing sacrificial hydrogen bonds through a simple bio-based additive is an effective strategy for designing UV-curable transparent coatings with outstanding low-temperature toughness and fire resistance.

Conflict of Interests

The authors declare no interest conflict.

Electronic Supplementary Information

Electronic supplementary information (ESI) is available free of charge in the online version of this article at http://doi.org/10.1007/s10118-026-3801-8.

Data Availability Statement

The data that support the findings of this study are available from the corresponding author upon reasonable request.

ACKNOWLEDGMENTS

The work was financially supported by the Opening Fund of State Key Laboratory of Fire Science (SKLFS) (No. HZ2024-KF15), the National Key Research and Development Program International Science and Technology Innovation Cooperation Special Project between Governments (No. 2025YFE0105800), and the Venture & Innovation Support Program for Chongqing Overseas Returnees (No. cx2022049).

REFERENCES

1 Yagci, Y.; Jockusch, S.; Turro, N. J. Photoinitiated polymerization: advances, challenges, and opportunities. *Macromolecules* **2010**, *43*, 6245−6260.
2 Zhao, L.; Li, Y.; Wei, Z.; Liang, J.; Ji, J.; Yan, S.; He, L. Photothermal self-lubricating anti-icing coating based on flower-like CuS and PDMS. *Prog. Org. Coat.* **2023**, *182*, 107666.
3 Zhang, W.; Feng, Z.; Chen, Z.; He, L.; Qi, L.; Hu, Y.; Gui, Z.; Xing, W. Phosphorus-nitrogen synergistic transparent UV-curable coatings to enhance the flame retardancy of polycarbonate. *Polym. Degrad. Stab.* **2024**, *225*, 110782.
4 Patil, R. S.; Thomas, J.; Patil, M.; John, J. To shed light on the UV curable coating technology: current state of the art and perspectives. *J. Compos. Sci.* **2023**, *7*, 513.
5 Dall Agnol, L.; Dias, F. T. G.; Ornaghi, H. L. Jr, Sangermano, M.; Bianchi, O. UV-curable waterborne polyurethane coatings: a state-of-the-art and recent advances review. *Prog. Org. Coat.* **2021**, *154*, 106156.
6 Morsy, A.; Kandil, S.; Ewais, H. A.; Abdel-Salam, A. H.; Mohamed, A. Eco-conscious flame retardants for enhanced fire resistance in natural fiber reinforced polymers composite: a review bio-based, and industry implications. *Chemosphere* **2025**, *377*, 144360.
7 Chen, X.; Hu, Y.; Jiao, C.; Song, L. Preparation and thermal properties of a novel flame-retardant coating. *Polym. Degrad. Stab.* **2007**, *92*, 1141−1150.
8 Sykam, K.; Hussain, S. S.; Sivanandan, S.; Narayan, R.; Basak, P. Non-halogenated UV-curable flame retardants for wood coating applications: review. *Prog. Org. Coat.* **2023**, *179*, 107549.
9 Ozman, E.; Dizman, C.; Birtane, H.; Kahraman, M. V. Novel bio-based phosphorous-containing UV-curable flame-retardant coatings. *J. Coat. Technol. Res.* **2023**, *20*, 1257−1268.
10 He, Z.; Xie, J.; Liao, Z.; Ma, Y.; Zhang, M.; Zhang, W.; Yue, H.; Gao, X. Hierarchical porous structure contained composite polyimide film with enhanced dielectric and water resistance properties for dielectric material. *Prog. Org. Coat.* **2021**, *151*, 106030.
11 Zhu, F.; Yan, X.; Lv, B.; Zhang, S.; Zeng, M.; Qiao, W. Balancing flame retardancy, mechanical properties, and transparency in epoxy resins with a phosphorus/sulfur-containing oligomer synthesized *via* thiol-ene click chemistry. *React. Funct. Polym.* **2026**, *219*, 106599.
12 Dou, Y.; Ju, A.; Zhong, Z.; Huo, Y.; Yao, W. Flame-retardant and transparent unsaturated polyester based on P/N liquid flame retardants and modified halloysite nanotubes. *Materials* **2024**, *17*, 761.
13 Pellerin, S.; Samyn, F.; Duquesne, S.; Landry, V. Preparation and characterisation of UV-curable flame retardant wood coating containing a phosphorus acrylate monomer. *Coatings* **2022**, *12*, 1850.
14 Patel, R.; Chaudhary, M. L.; Patel, Y. N.; Chaudhari, K.; Gupta, R. K. Fire-resistant coatings: advances in flame-retardant technologies, sustainable approaches, and industrial implementation. *Polymers* **2025**, *17*, 1814.
15 Azani, M.-R.; Hassanpour, A. UV-curable polymer nanocomposites: material selection, formulations, and recent advances. *J. Compos. Sci.* **2024**, *8*, 441.
16 Xie, D.; Lansana, A. M.; Nuermaimaiti, X.; Kang, Q.; Chen, F.; Jiang, B.; Gao, J.; Song, P.; Dai, J. Making polycarbonate flame retardant and transparent: current advances and future challenges in flame retardant selection and mechanisms. *Polym. Degrad. Stab.* **2025**, *241*, 111607.
17 Chen, Y.; Bian, Z.; Wei, Y.; He, X.; Lu, X.; Lu, Q. Polyhedral oligomeric silsesquioxanes (POSS) for transparent coatings: material properties and applications. *Polymers* **2025**, *17*, 3050.
18 Pugliese, D.; Malucelli, G. Toward the optimization of the optical behavior of transparent wood: current state of the art and perspectives. *Polymers* **2025**, *17*, 3276.
19 Mettry, M. Y.; Lighty, A. M.; Hammons, J. A.; Malone, D. R.; Bertsch, K. M.; Fears, T. M. Transparent polyimide aerogels: controlled porosity *via* minimizing the phase separation. *ACS Appl. Polym. Mater.* **2022**, *4*, 8065−8072.
20 Czachor-Jadacka, D.; Pilch-Pitera, B. Progress in development of UV curable powder coatings. *Prog. Org. Coat.* **2021**, *158*, 106355.

Graphical Abstract

Transparent UV Cured Coatings Enabled by Biomass Phytic Acid with Enhanced Flame Retardancy and Low Temperature Toughness

Yu Yu, Sheng-Hua Yang, Hong-Yu Yuan, Feng Liu, Xia-Ming Feng, Hong-Yu Yang, and Chao-Jun Wan

Chongqing University

Biomass derived phytic acid constructs sacrificial H-bond networks in transparent UV curable coatings, overcoming flame retardancy-toughness trade-off with UL-94 V-0 rating and improved low temperature toughness.

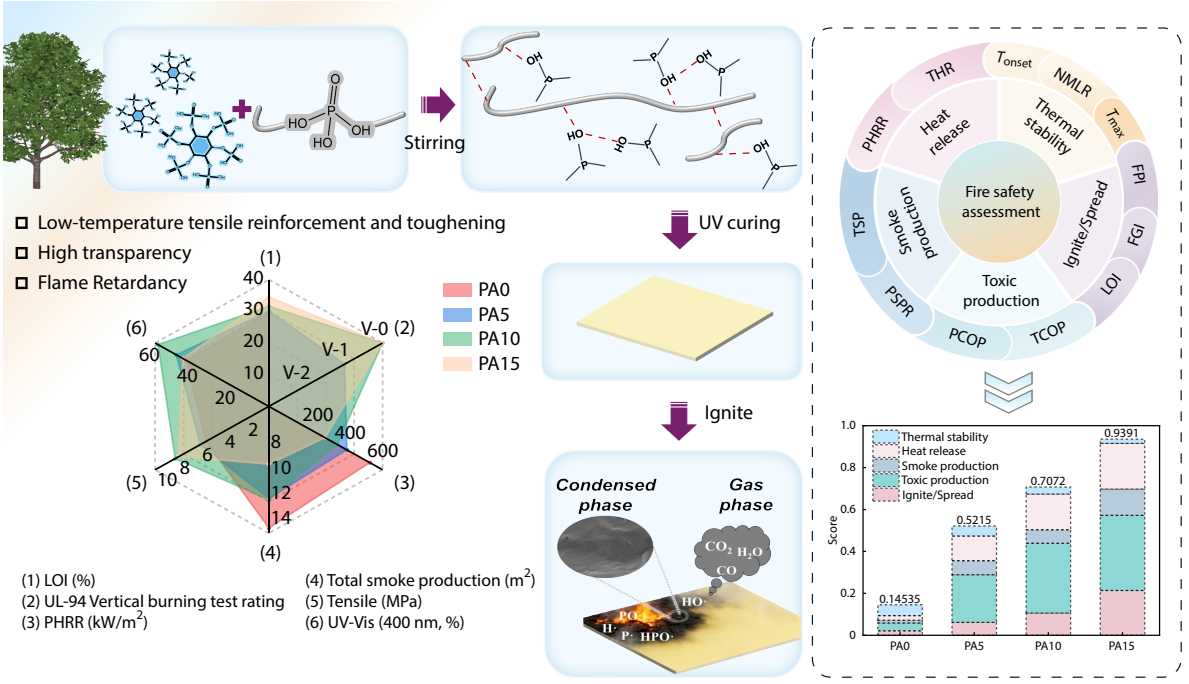

Chinese J. Polym. Sci. 2026 *https://doi.org/10.1007/s10118-026-3801-8*

21 Kurdikar, D. L.; Peppas, N. A. A kinetic study of diacrylate photopolymerizations. *Polymer* **1994**, *35*, 1004–1011.
22 Meng, Q.; Liu, S.; Yu, Y.; Gong, X.; Wang, B.; Ma, J.; Han, S. UV-curable, self-healing and rigid polyurethane-urea acrylate elastomers reinforced with zirconium phosphate nanosheets. *ACS Appl. Polym. Mater.* **2026**, *8*, 2815–2830.
23 Vinodhini, S. P.; Xavier, J. R.; Priyadharshini, A. A review on flame retardant, anticorrosion, and mechanical properties of multifunctional polymer nanocomposite coatings for industrial applications. *Prog. Org. Coat.* **2025**, *206*, 109361.
24 Li, Y.; Niu, H.-X.; Jiang, H.-R.; Ma, C.; Yan, Y.; Shi, H.-J.; Zhou, K.-S.; Hu, Y.; Wang, X. Cardanol-derived phosphorus-containing acrylates as UV-curable, highly transparent and flame retardant coatings for polycarbonate. *Ind. Crops Prod.* **2025**, *233*, 121386.
25 Ye, G.; Huo, S.; Wang, C.; Guo, Y.; Yang, Q.; Song, P.; Wang, H.; Liu, Z. A transparent epoxy vitrimer with outstanding flame retardancy, toughness, and recyclability enabled by a hyperbranched P/N-derived polyester. *Constr. Build. Mater.* **2025**, *489*, 140673.
26 Zhang, L.; Zhang, A. N.; He, S. M.; Zheng, G. Q.; Zeng, F. R.; Wang, Y. Z.; Liu, B. W.; Zhao, H. B. Biomimetic nanoporous transparent universal fire-resistant coatings. *ACS Appl. Mater. Interfaces* **2024**, *16*, 19519–19528.
27 Ma, X.; Yun, H.; Wu, N.; Niu, F.; Yu, J. Superior water-resistant poly (2-hydroxyethyl methacrylate phosphate) flame retardant and a transparent, flame-retardant, and biodegradable poly(lactide) blend film. *ACS Appl. Polym. Mater.* **2021**, *3*, 1314–1323.
28 Huang, B.; Li, G.; Zhang, H.; Qu, J.; Sun, W.; Liu, L.; Liu, M.; Li, S.; Jiao, C.; Zhao, X.; Chen, X. An eco-friendly flame retardant from chitosan, phytic acid, Fe-MOF endows thermoplastic polyurethane with enhanced fire safety and mechanical property based on hydrogen bond and π-π stacking. *Int. J. Biol. Macromol.* **2025**, *310*, 143139.
29 Andrzejewska, E. Photopolymerization kinetics of multifunctional monomers. *Prog. Polym. Sci.* **2001**, *26*, 605–665.
30 Colanges, S.; Ballu, K.; Lamouroux, A.; Pecastaings, G.; Ly, I.; Le Coz, C.; Tassaing, T.; Brunet, T.; Grau, E.; Cramail, H.; Mondain-Monval, O.; Vidil, T. Spatio-temporal investigation of the crosslinking and the mechanical properties in a UV-curable rubber bearing photo-dimerizable moieties. *Eur. Polym. J.* **2025**,

223, 113655.
31 Li, B.; Hao, W.; Wu, A.; Zhou, M.; Yan, Q.; Zhang, H.; Su, L. Preparation and characterization of PA/P(AA-*co*-AM) composite hydrogels *via* photopolymerization. *RSC Adv.* **2023**, *13*, 22831−22837.
32 Feng, X.; Li, G. Versatile phosphate diester-based flame retardant vitrimers *via* catalyst-free mixed transesterification. *ACS Appl. Mater. Interfaces* **2020**, *12*, 57486−57496.
33 Yang, S.; Guo, J.; Yuan, H.; Xiao, H.; Feng, X.; Yang, H.; Yan, C.; Cai, W. Eco-friendly ternary synergistic P/N/B intumescent flame-retardant uv-curable coating with enhanced thermal stability and smoke suppression. *Prog. Org. Coat.* **2026**, *211*, 109834.
34 Noda, I. Generalized two-dimensional correlation spectroscopy. in *Frontiers of Molecular Spectroscopy*. Amsterdam: Elsevier, **2009**, pp. 367−381.
35 Deng, K.; Zhang, A.; Feng, X.; Yang, H.; Wan, C.; Yan, C. Solvent-free mechanochemistry induced one-pot scalable fabrication of phosphorus wrapped keratin and its application as a synergistic flame retardant in epoxy resin. *Compos. Part A Appl. Sci. Manuf.* **2025**, *189*, 108622.
36 Yu, B.; Liu, M.; Lu, L.; Dong, X.; Gao, W.; Tang, K. Fire hazard evaluation of thermoplastics based on analytic hierarchy process (AHP) method. *Fire Mater.* **2010**, *34*, 251−260.
37 Schartel, B.; Hull, T. R. Development of fire-retarded materials—Interpretation of cone calorimeter data. *Fire Mater.* **2007**, *31*, 327−354.
38 Saaty, T. L. How to make a decision: the analytic hierarchy process. *Eur. J. Oper. Res.* **1990**, *48*, 9−26.
39 Jahan, A.; Edwards, K. L. A state-of-the-art survey on the influence of normalization techniques in ranking: improving the materials selection process in engineering design. *Mater. Des. (1980-2015)* **2015**, *65*, 335−342.
40 Fang, Y.; Zhou, Y.; Yang, Z.; Liu, C.; Liu, Q.; Yang, X.; Zheng, P. A synergistic phosphorus-nitrogen flame retardant containing both oxazine ring and biphenyl structures effectively addresses the flame retardancy and char formation issues in epoxy resins. *Polymer* **2026**, *344*, 129512.
41 Sun, R.; Hu, D.; Zhang, G.-R.; Sun, D.-X.; Wang, Y. Intumescent flame-retardant coatings on polyurethane foam *via* layer-by-layer assembly: the role of assembly sequence in enhancing performance. *Appl. Surf. Sci.* **2026**, *726*, 165851.
42 Lai, J.; Chen, Y.; Liu, F.; Yi, Z.; Ding, F.; Ren, X. A facile method for flame retardant and mechanically reinforced PET fabrics based on sustainable components. *ACS Appl. Polym. Mater.* **2026**, *8*, 2067−2076.
43 Li, J.; Zhang, J.; Jiang, J.; Xiang, W.; Xia, S.; He, G.; Fu, Z.; Wang, T.; An, W.; Chen, M.; Deng, J. Durable flame-retarding and antifouling cotton fabrics based on hydrophobic protection coating. *J. Appl. Polym. Sci.* **2026**, *143*, e58187.
44 Shi, J.; Song, X.; Wang, F.; Chen, J.; Wang, Y.; Wang, X.; Liu, Y. Phosphorus- and nitrogen-bridged chitooligosaccharide as an effective flame-retardant coating of fiber cardboard. *ACS Sustainable Chem. Eng.* **2025**, *13*, 3413−3422.
45 Di, X.; Chen, X.; Kang, Y.; Yang, J.; Zou, Y.; Jing, J.; Sun, J.; Li, H.; Gu, X.; Zhang, S. Introducing a polysiloxane coating on flame retardant to realize durable UV resistance and flame retardancy of polypropylene. *Polym. Degrad. Stab.* **2025**, *239*, 111403.
46 Triantaphyllou, E.; Sánchez, A. A sensitivity analysis approach for some deterministic multi-criteria decision-making methods. *Decis. Sci.* **1997**, *28*, 151−194.

https://doi.org/10.1007/s10118-026-3801-8